The Astrophysical Journal, 983:143 (14pp), 2025 April 20 https://doi.org/10.3847/1538-4357/adc12a

Minifilament Eruptions as the Last Straw to Break the Equilibrium of a Giant Solar Filament

Hechao Chen[1,2,3], Hui Tian[2], Quanhao Zhang[4], Chuan Li[5,6], Chun Xia[1,3], Xianyong Bai[7], Zhenyong Hou[2], Kaifan Ji[8], Yuanyong Deng[7], Xiao Yang[7], and Ziyao Hu[7]

[1] School of Physics and Astronomy, Yunnan University, Kunming, 650500, People's Republic of China; hechao.chen@ynu.edu.cn
[2] School of Earth and Space Sciences, Peking University, Beijing, 100871, People's Republic of China; huitian@pku.edu.cn
[3] Yunnan Key Laboratory of the Solar Physics and Space Science, Kunming, 650216, People's Republic of China
[4] CAS Key Laboratory of Geospace Environment, Department of Geophysics and Planetary Sciences, University of Science and Technology of China, Hefei, 230026, People's Republic of China
[5] School of Astronomy and Space Science, Nanjing University, Nanjing 210023, People's Republic of China
[6] Institute of Science and Technology for Deep Space Exploration, Suzhou Campus, Nanjing University, Suzhou 215163, People's Republic of China
[7] National Astronomical Observatories, Chinese Academy of Sciences, Beijing, 100101, People's Republic of China
[8] Yunnan Observatories, Chinese Academy of Sciences, 396 Yangfangwang, Guandu District, Kunming, 650216, People's Republic of China
Received 2025 February 13; revised 2025 March 13; accepted 2025 March 14; published 2025 April 16

Abstract

Filament eruptions are magnetically driven violent explosions commonly observed on the Sun and late-type stars, sometimes leading to monster coronal mass ejections that directly affect the nearby planets' environments. More than a century of research on solar filaments suggests that the slow evolution of photospheric magnetic fields plays a decisive role in initiating filament eruptions, but the underlying mechanism remains unclear. Using high-resolution observations from the Chinese Hα Solar Explorer, the Solar Upper Transition Region Imager, and the Solar Dynamics Observatory, we present direct evidence that a giant solar filament eruption is triggered by a series of minifilament eruptions occurring beneath it. These minifilaments, which are homologous to the giant filament but on a smaller tempo-spatial scale, sequently form and erupt due to extremely weak mutual flux disappearance of opposite-polarity photospheric magnetic fields. Through multifold magnetic interactions, these erupting minifilaments act as the last straw to break the force balance of the overlying giant filament and initiate its ultimate eruption. The results unveil a possible novel pathway for small-scale magnetic activities near the stellar surface to initiate spectacular filament eruptions, and provide new insight into the magnetic coupling of filament eruptions across different tempo-spatial scales.

Unified Astronomy Thesaurus concepts: Solar physics (1476); Solar activity (1475); Solar magnetic fields (1503); The Sun (1693); Solar filaments (1495); Solar coronal mass ejections (310); Solar magnetic reconnection (1504)

Materials only available in the online version of record: animations

1. Introduction

Filaments are one type of magnetized plasma structures commonly observed in the coronae of solar-like and later-type stars (A. Collier Cameron 1996). These unique phenomena are the key to uncovering the intricate interplay between astrophysical magnetic fields and plasmas in the universe. Filaments, also known as stellar prominences when appearing above the stars' limb, usually come to an end through magnetically driven eruptions. Once erupting, they are most likely accompanied by flares and spectacular coronal mass ejections (CMEs) with a rapid magnetic energy release (P. F. Chen 2011; K. Shibata & T. Magara 2011; B. Schmieder et al. 2013), which may adversely affect the nearby orbiting planets and even pose a threat to their habitability (V. S. Airapetian et al. 2020; H. Tian et al. 2023).

On the Sun, filaments have been studied for over a century with spatially resolved observations due to their proximity (S. Parenti 2014). Extensive solar observations have shown that filaments form and erupt from the sunspot belts to the polar crown (J. Jing et al. 2004; Y. Su & A. van Ballegooijen 2012), with timescales ranging from minutes to months and lengths spanning from $\sim 10^3$ km up to 10^5 km (J. Wang et al. 2000; J. Hong et al. 2011; N. K. Panesar et al. 2017; H. Chen et al. 2020). Their eruptions exhibit a very broad energy releasing range (10^{25}–10^{32} erg) and a wide mass ejection range (10^{12}–10^{15} g) (Y. Kotani et al. 2023). The scale-free self-similar nature of magnetohydrodynamics (MHD) suggests that these multi-scale filaments are cross-scale analogs that form via a common mechanism (H. Chen et al. 2020). Moreover, a few studies state that solar eruptive activities driven by filaments at different scales, including stellar-scale CMEs and small-scale coronal jets, may also be triggered by a similar mechanism (N. E. Raouafi et al. 2010; C. J. Schrijver 2010; A. C. Sterling et al. 2015; P. F. Wyper et al. 2017), but the conditions that make filament eruptions inevitable remain a subject of active debate (G. Aulanier 2014, 2021). Observations and numerical simulations of filament eruptions over the past decades have suggested that the slow evolution of photospheric magnetic fields plays a decisive role in initiating filament eruptions. Many possible mechanisms, i.e., breakout (S. K. Antiochos et al. 1999; P. F. Wyper et al. 2017) and tether-cutting reconnection (R. L. Moore et al. 2001; C. Jiang et al. 2021), as well as ideal MHD instabilities (T. G. Forbes & P. A. Isenberg 1991; T. Török et al. 2004; B. Kliem & T. Török 2006), have been proposed to explain the initiation of filament eruptions.

However, all of these models concentrate exclusively on the eruption of individual filaments within specific spatial-temporal scales, which prevents us from uncovering the potential physical connections between filament eruptions across different spatial-temporal scales.

Here, we report the discovery of a new type of physical coupling between miniature and giant filament eruptions along the same polarity inversion line (PIL), which has never been considered in current theories and observations. Minifilament eruptions driven by extremely weak photospheric flux cancellation are found to act as the last straw to break the initial equilibrium of an overlying giant filament through multifold magnetic interactions. This finding represents the first solid evidence that large-scale filament eruptions could be triggered by similar eruptions at much smaller scales, opening a new window to understanding the physical connection among different filament eruptions across different tempo-spatial scales. Moreover, this unique coupling-eruption pattern is found to be driven by a nonuniform photospheric flux cancellation process. By incorporating the nonuniform characteristics of actual photospheric magnetic flux cancellation, we successfully interpret all crucial features of this unique coupling-eruption pattern of miniature and giant filaments into a unified physical framework, and add new and significant elements into the traditional flux cancellation model (A. A. van Ballegooijen & P. C. H. Martens 1989).

2. Instruments

The giant filament eruption of interest occurred near the southwest limb of the solar disk. It caused a C-class flare and notable coronal dimming in its source region, as well as an accompanying CME in the higher corona. Several space-borne observatories, including the Chinese Hα Solar Explorer (CHASE; C. Li et al. 2022), the Solar Upper Transition Region Imager (SUTRI; X. Bai et al. 2023), and the Solar Dynamics Observatory (SDO; W. D. Pesnell et al. 2012), as well as the Solar TErrestrial RElations Observatory (STEREO; R. A. Howard et al. 2008), have well recorded the activation and eruption of this event. This allows us to investigate the triggering process of the giant filament in detail.

The SUTRI is China's first telescope to probe the solar transition region and is one of the payloads on board the first spacecraft of the Space Advanced Technology demonstration satellite series, which was launched in 2022 July. As a low-cost experiment, SUTRI aims to test the on-orbit performance of EUV CMOS imaging camera and Sc/Si multilayer reflecting mirror. SUTRI observes the full solar disk and samples plasma at a temperature of 0.5 MK (H. Tian 2017) using the Ne VII 465 Å line, with a time cadence of 30 s and a spatial resolution of $\sim 8''$. This unique passband has rarely been used by past and existing solar extreme ultraviolet imagers. In recent years, SUTRI has contributed to research on solar eruptive events, achieving a wealth of research results (e.g., Y. Hou et al. 2023; D. Li et al. 2023; L. Li et al. 2023; Z. Sun et al. 2023; Z. Hou et al. 2024; Q. M. Zhang et al. 2024; X. Zhou et al. 2024). The filament eruption under our study was one of the most interesting events captured by SUTRI after it started routine observations on 2022 September 4. SUTRI Level 0.9 465 Å images were used to investigate the dynamics of this filament eruption.

The CHASE, dubbed as "Xihe" in Chinese (the Goddess of the Sun in China), was launched into a Sun-synchronous orbit on 2021 October 14. As the scientific payload of CHASE, the Hα Imaging Spectrograph (HIS), for the first time, acquires seeing-free Hα solar spectroscopic observation with high temporal and spectral resolutions. The CHAE/HIS performs its routine observations in two modes: raster scanning mode (RSM) and continuum imaging mode. In our study, the RSM Level 1 Hα (6559.7−6565.9 Å) spectra under the full Sun scanning mode were used to investigate the dynamics of the filament eruption and its precursor activity, with a temporal resolution of about 1 minute and a pixel spectral resolution of 0.024 Å. The Level 1 RSM spectra were produced from the Level 0 data via a detailed calibration procedure (Y. Qiu et al. 2022), which include dark-field and flat-field correction, slit image curvature correction, wavelength, and intensity calibration, as well as coordinate transformation. The CHAE/HIS Hα spectra were utilized to reconstruct two-dimensional (2D) Doppler maps using a weight-inverse-intensity method. To eliminate the effects of solar rotation and satellite motion, a reference line profile was obtained by averaging spectra from a nearby quiet region. This reference line profile was then employed for rest wavelength calibration. It is important to note that the CHASE observational data for this event contains some time gaps. Therefore, GONG Hα data was used as a supplement to construct the time–distance plot.

The Atmospheric Imaging Assembly (AIA; J. R. Lemen et al. 2012) on board the SDO observes the full solar disk in 10 EUV and UV passbands, with a spatial pixel size of $\sim 0.''6$ and a time cadence of 12 s in EUV passbands (24 s in UV passbands). The Helioseismic and Magnetic Imager (HMI; P. H. Scherrer et al. 2012) on board the SDO measures the full-disk solar photospheric magnetic field at six wavelength positions across the Fe I 6173 Å spectral line. Here, AIA images in 304, 171, and 193 Å passbands were used to investigate the plasma dynamics during the filament eruption, and the HMI light-of-sight (LOS) magnetograms were employed to inspect the photospheric magnetic field evolution beneath the eruption. The SUTRI and SDO data were reduced using the standard analysis tool available in the SolarSoftWare IDL (SSWIDL) package. To compensate for the solar rotation, all the SDO and SUTRI images taken at different times are aligned to an appropriate reference time.

3. Observations and Results

3.1. Overview

According to the long-term CHASE Hα and HMI LOS magnetogram monitor (Figure A1), this giant quiescent filament appeared in an unnamed active region remnant since 2022 September 11. It exhibited prominent barbs and an apparent length exceeding 300 Mm. From September 8 to 16, long-term photospheric flux cancellation persistently occurred at the core of the active region remnant along the PIL of the giant filament. This cancellation exhibited a gradual reduction in the spatial scale, shrinking from the initial active region size to a few Mm. In this course, the giant filament remained relatively stable for the first several days, and its middle segment became highly diffuse in Hα images starting from September 13. The giant filament eventually erupted at approximately 20:00 UT on September 15. Before its final eruption, a series of preceding small-scale eruptive activities occurred below its middle segment during 15:00–19:00 UT (see the associated movie in Figure 1). At first sight, these small-scale eruptions appeared to disturb the magnetic fields of

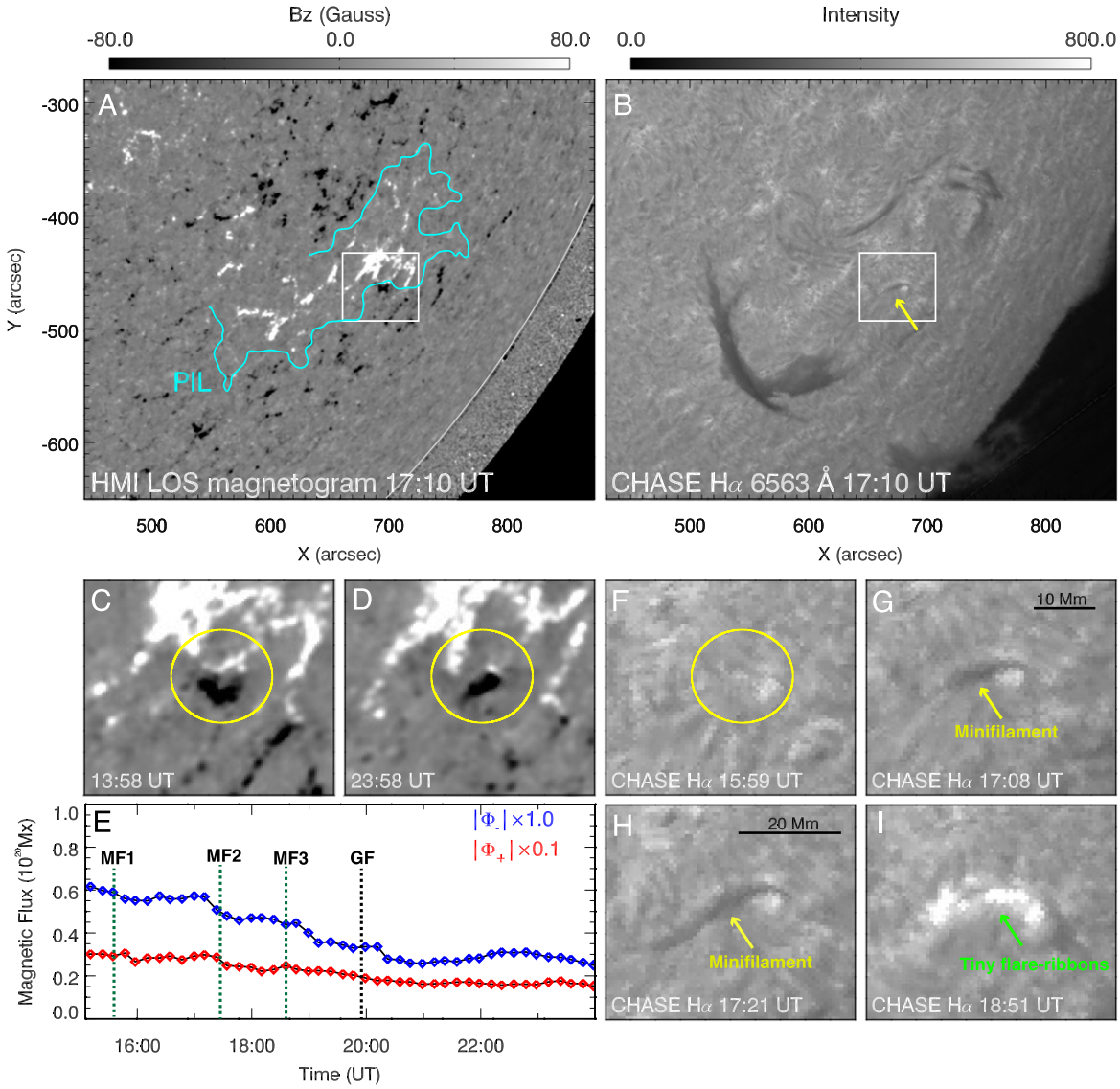

Figure 1. The formation and eruption of minifilaments underneath a giant filament due to small-scale flux cancellation on September 15. (A) The SDO/HMI LOS magnetogram at 17:10 UT. The cyan solid line denotes the PIL where both the minifilaments and giant filament form. (B) The CHASE Hα image at 6562.8 Å. (C)–(D) The convergence and cancellation of opposite-polarity small-scale magnetic flux concentrations. Another unrelated prominence is observed at the limb ($x = 730$, $y = -600$) and remains stable during the giant filament eruption. The field of view (FOV) is indicated by the white rectangle in (A). (E) Evolution of magnetic flux during 15:00−24:00 UT within the FOV of (C). Four vertical dashed lines indicate the eruption times of three minifilaments (abbreviated as MF1, MF2, and MF3) and the overlying giant filament (abbreviated as GF), respectively. (F)–(I) Snapshots of minifilament activity in the FOV of (C). Features of interest are marked in each panel; see the text for details. An animation of panel (A) is available in the online journal. The animation also includes the AIA 193 Å image sequence (bottom panel). This animation presents a time sequence of 720 s spanning from 15:34 UT to 23:58 UT on 2022 September 15, with a total real-time duration of 10 s.

(An animation of this figure is available in the online article.)

the overlying giant filament, potentially triggering its subsequent eruption.

3.2. Minifilaments and Extremely Weak Flux Cancellation Beneath the Giant Filament

Thanks to the unprecedented seeing-free Hα observation by CHASE, we clearly see that these small-scale eruptive activities below the pre-eruption giant filament are a sequence of homologous minifilament eruptions. In the CHASE Hα image taken at 17:08 UT, it is clear that one minifilament existed right below the middle section of the pre-eruption giant filament (Figure 1(B)). The simultaneous HMI LOS magnetogram shows that this minifilament and the giant filament resided along the same filament channel (or PIL) (Figure 1(A)). This unique magnetic configuration of coexisting mini- and giant filaments is reminiscent of the reported double-decker magnetic flux rope (MFR) system in active region filaments (R. Liu et al. 2012). Based on filament chirality rules, we find that the giant filament should be supported in an MFR configuration with a sinistral chirality (methods in Appendix A). The nonlinear force-free field (NLFFF) extrapolations based on the vector photospheric magnetic measurements reveal that the minifilament also resided in a sinistral small-scale MFR (Figure A1; methods in Appendix A).

The photospheric source region of this minifilament is a small-scale mixed-polarity region, locating at the middle section of the whole curved PIL (see the white box in Figures 1(A) and (B)). In this region, opposite-polarity

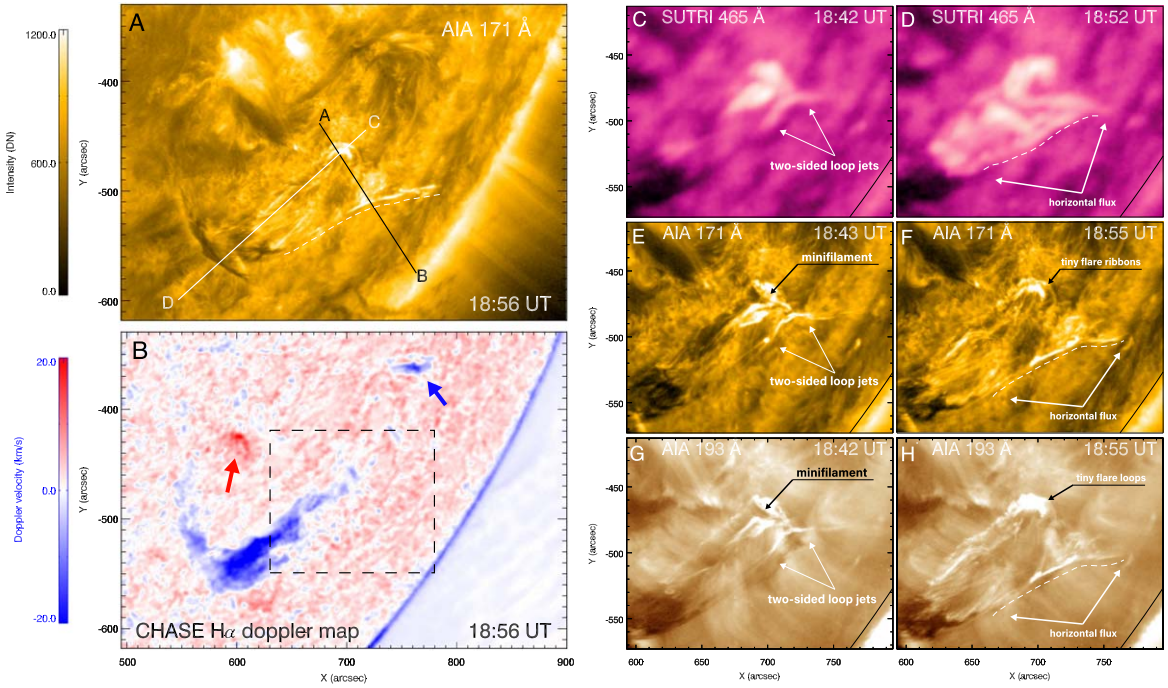

Figure 2. Magnetic interaction between the erupting minifilament and the overlying giant filament during the period from 18:30 UT to 19:30 UT on 2022 September 15. (A) The AIA 171 Å image at 18:56 UT. The solid lines AB (in black) and CD (in white) indicate the slice positions for the two spacetime diagrams in Figure 4, respectively. The white dashed line outlines a bundle of upward-moving horizontal magnetic field or flux. (B) The Doppler map reconstructed from the CHASE Hα spectroscopic observation at 18:56 UT. The red/blue arrow marks the redshift/blueshift at the left/right feet of the erupting giant filament, respectively. The black dashed rectangle represents the FOV of (C)–(H). (C)–(H) Zoom-in snapshots of the magnetic interaction process in SUTRI 465, AIA 171, and AIA 193 Å images. Features of interest are marked in each panel; see the text for details. An animation of this figure is available in the online journal, showing the interaction between the erupting minifilament and the giant filament. The animation runs from 18:00 to 19:20 in the AIA 171 Å sequence and similar times in the other panels. The real-time duration of the animation is 3 s.

(An animation of this figure is available in the online article.)

magnetic flux concentrations underwent a very slow and long-lasting convergence and cancellation at a very short section of the PIL on September 15 (yellow circles in Figures 1(C) and (D) and associated movie). The magnetic flux cancellation refers to the mutual approach and subsequent disappearance of opposite-polarity magnetic fragments in the photosphere (see references in C. Zwaan 1987). From 14:00 to 21:00 UT on September 15, the total reduction of negative flux is $\sim 3.1 \times 10^{19}$ Mx and the rate of flux cancellation is $\sim 2.6 \times 10^{18}$ Mx hr^{-1} on average. The boundary of canceling opposite magnetic polarities provides a necessary environment for the buildup of filament magnetic fields (S. F. Martin 1998a; D. H. Mackay et al. 2010). During this extremely weak flux cancellation, three homologous minifilaments sequently formed within 10−30 minutes, and erupted above this canceling site at 15:30 UT, 17:30 UT, and 18:40 UT, respectively (refer to the eruption times of these minifilaments that are marked in Figure 1(E)). Assuming that an equal amount of positive and negative flux cancels and all canceled flux builds the minifilament magnetic field within 10 to 30 minutes, we can roughly estimate that $\sim(0.87–2.6) \times 10^{18}$ Mx of magnetic flux contributes to the buildup of each minifilament on average. This kind of canceled flux is a minuscule fraction of the total magnetic flux of the whole giant filament channel (about $\sim 6.8 \times 10^{21}$ Mx). The CHASE observation covered the formation of the second minifilament (see Figures 1(F) to (H)) and the eruption of the third one (Figure 1(I)). As shown in Figures 1(G) and (H), the second minifilament had a projected length of about 10 Mm at the very beginning of its birth at 17:08 UT, and soon it grew to 20 Mm near its eruption at 17:21 UT. Though these minifilaments are very short-lived features formed and erupted on a timescale of only tens of minutes, their eruptions continuously disturbed the overlying giant filament (see Figures 2 and 3(B) and (C)).

3.3. Activation of the Giant Filament Due to Minifilament Eruptions

Solid evidence of magnetic interaction occurring between the third erupting minifilament and the giant filament was shown in Figure 2 and the associated movie. This minifilament eruption occurred at about 18:40 UT and caused tiny chromospheric flare ribbons (Figures 1(I) and 2(F)). At about 18:42 UT, the erupting minifilament structure lifted up and directly reconnected with the overlying giant filament fields. As a result of this reconnection, their interaction site soon radiated enhanced EUV emission, which can be simultaneously detected in almost all the AIA EUV passbands and the SUTRI 465 Å passband (Figures 2(C), (E), and (G)). At the same time, a pair of roughly antiparallel plasma beams soon developed from the central emission region, forming a series of so-called two-sided loop jets or bidirectional jets (e.g., Y. Jiang et al. 2013; R. Zheng et al. 2018; Y. Shen et al. 2019; A. C. Sterling et al. 2019; S. Tan et al. 2023). The bidirectional jets occurred at the interface between the overlying giant filament and the erupting minifilament, $\sim$24 Mm above the photosphere (see Figure 3(D); methods in Appendix B). The projected velocities of the bidirectional jets were measured using a time–distance analysis and found to be $\sim$134 km s^{-1} and 54 km s^{-1},

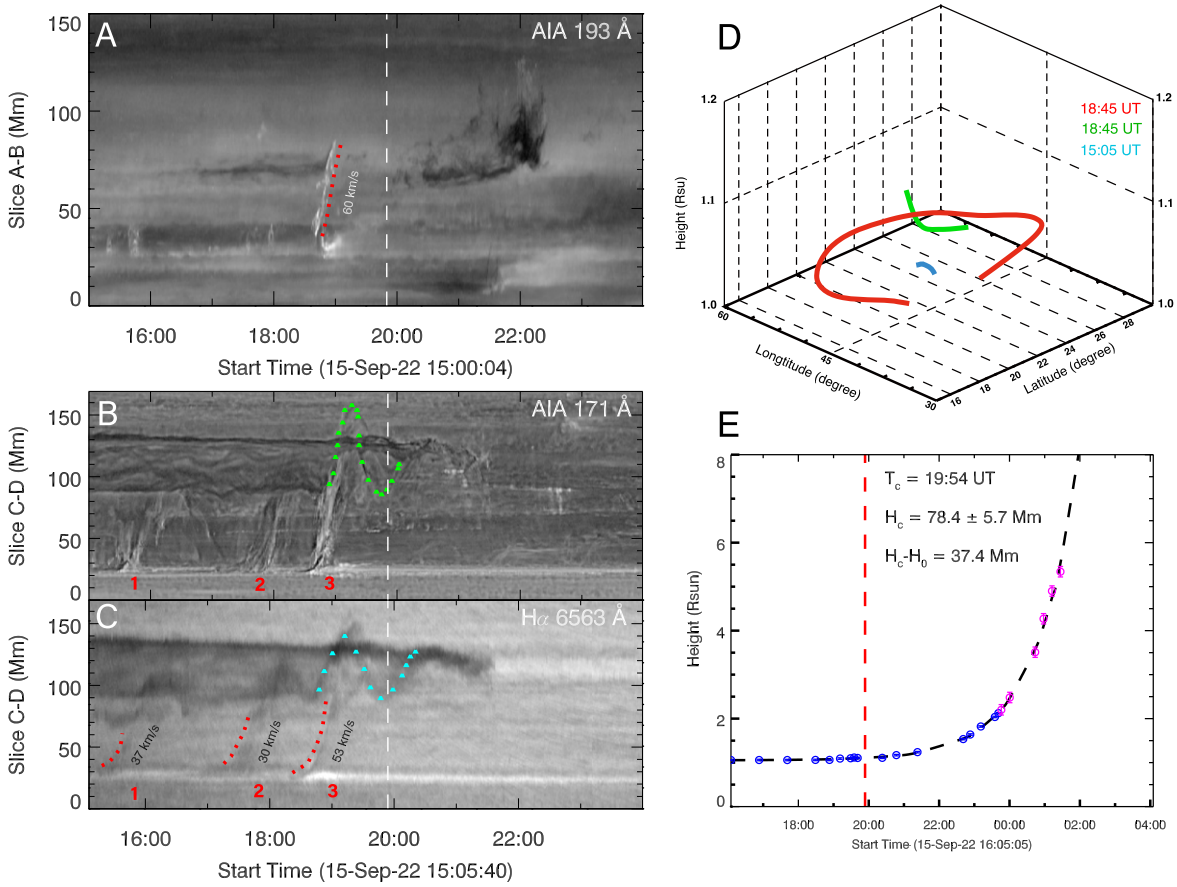

Figure 3. Eruptive dynamics and 3D reconstruction of the giant filament. (A) Space–time diagram of AIA 193 Å images along slice AB in Figure 2(A). The red-dotted line highlights an upward-moving horizontal flux feature, and its moving velocity is around 60 km s^{-1}. (B), (C) Space–time diagrams of AIA 171 Å and GONG Hα images along slice CD in Figure 2(A), respectively. Three minifilament eruptions are marked by red numbers (1, 2, 3), respectively. Their velocity are fitted to be 37 km s^{-1}, 30 km s^{-1}, and 53 km s^{-1}, respectively. The green/cyan diamonds highlight the plasma oscillation (amplitude ~50–70 Mm) of the giant filament near its southern part. (D) The 3D morphology of minifilament (blue), giant filament (red), and two-sided loop jets (green) reconstructed through stereoscopic observations of STEREO-A/EUVI and SDO/AIA in 304 Å passbands. (E) Height of the main axis top of the erupting giant filament as a function of time and its fitting result (black dashed line). The blue dots represent stereoscopic measurements from SDO/AIA and STEREO/EUVI, and the purple dots are measured from LASCO/C2. The white dashed lines in (A)–(C) and the red dashed line in (E) indicate the fitted onset time (19:54 UT) of the giant filament eruption.

respectively. The higher southward velocity is likely due to a less pronounced projection effect.

Several minutes later, a series of newly formed horizontal bright thread-like plasma structures were developed and then detached from the bidirectional jet spires, which can be clearly observed in both 171 and 193 Å, as well as 465 Å passbands (see Figures 2(A), (D), (F), and (G) and associated movie). Later on, they rapidly ascended upward and eventually merged into the overlying giant filament, with a projected velocity of ~60 km s^{-1} (Figure 3(A)). Considering the high magnetic Reynolds number of the hot corona, the plasma is frozen to the magnetic field, so these ascendent thread-like plasma structures very likely trace out a series of upward-transporting horizontal magnetic fields from the minifilament eruption. Owing to the horizontal magnetic field merging into the overlying giant filament structure and the mass ejection from bidirectional jets, enhanced mass flows immediately appeared as evident blueshifts along the giant filament axis in the simultaneous CHASE Hα Doppler map (Figure 2(B) and associated movie). At the two ends of the giant filament, enhanced mass flows caused patchy blueshift and redshift signals along the LOS, respectively. Due to enhanced mass flows, possible mass drainage may facilitate the lift of the giant filament by reducing its filament weight (e.g., Y. Fan 2018). After this sudden activation process, the giant filament soon stepped into its eruption phase at about 20:00 UT.

3.4. The Last Straw to Break the Quasi-static Equilibrium of the Giant Filament

With the aid of three-dimensional (3D) stereoscopic reconstruction (see Figure B1 and methods in Appendix B), we find that the height–time profile of the giant filament consists of a slow-rise phase and a rapid-acceleration phase (Figure 3(E)). This profile can be well characterized by a fitting function consisting of linear and exponential components (fitting methods in Appendix B). The fitting result reveals that (1) the slow-rise phase of the giant filament began at ~16:00 UT (which coincided with the first eruption of the minifilament) and its ascent velocity is quite slow (~4−6 km s^{-1}), indicating a quasi-static evolution; (2) the giant filament suddenly erupted upward with a velocity of ~140 km s^{-1} and the onset time of the rapid-acceleration phase is about 19:54 UT. This acceleration process was accompanied by a solar flare, showing up as a simultaneous AIA 171 Å flux enhancement in its coronal source region (Figure B2(E) and associated movie). These results suggest that the giant filament eruption was related to a quasi-static evolution and then a flare-related energy releasing process (e.g., X. Cheng et al. 2020).

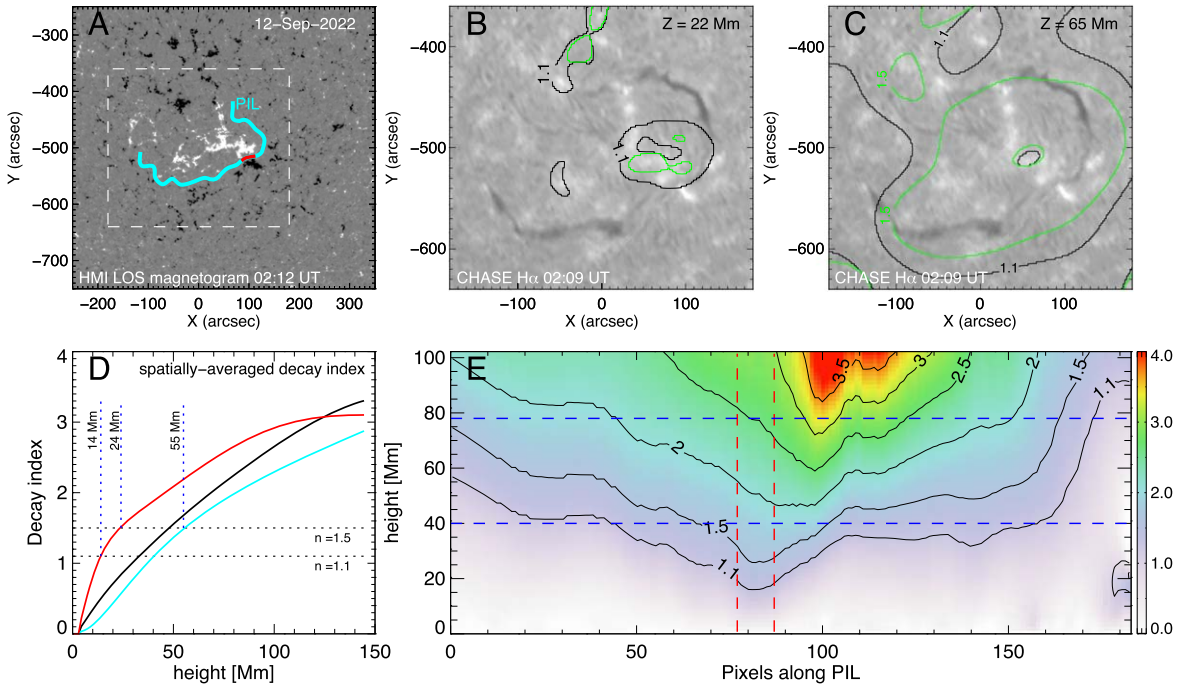

Figure 4. Magnetic decay index analysis above the PIL of miniature and giant filaments on 2022 September 12. (A) Magnetic environment of the source region, as it passed the central meridian on 2022 September 12. PILs of the whole filament channel and of the minifilaments are outlined by the cyan and red lines, respectively. (B) and (C): 2D spatial distributions of decay index at the heights of 22 Mm and 65 Mm are plotted over a simultaneously taken CHASE Hα image, respectively. (D) Spatially averaged decay index as a function of height, which respectively are calculated over the whole PIL, the minifilament-related PIL (red section in (A)), as well as the rest PIL (two cyan sections in (A)). (E) The height variation of decay index above the whole PIL at 02:12 UT, in which contours at different levels are also plotted. Two red dashed vertical lines highlight the corresponding spatial range right above the PIL of minifilaments. Two blue-dashed horizontal lines indicate the initial and maximum heights of the pre-eruption giant filament.

To understand the abrupt kinematic transition from the quasi-static evolution to the rapid acceleration, we present time–distance diagrams along slices AB and CD in Figure 2(A). These diagrams allow a quantitative investigation for the dynamic response of the giant filament to horizontal magnetic field merging and mass ejections from multiple minifilament eruptions, respectively. The time–distance diagram along slice AB in AIA 193 Å images (Figure 3(A)) clearly shows that during the third minifilament eruption, obvious horizontal flux moving along with the erupting minifilament merged into the overlying giant filament. The time–distance diagrams along slice CD in AIA 171 Å and Hα images (Figures 3(B) and (C)) consistently reveal that due to the mass ejections from three subsequent minifilament eruptions, the giant filament was remarkably disturbed and its cross section underwent an apparent compression. The third minifilament eruption, as the strongest one with a projected eruption velocity of 53 km s^{-1}, caused a very prominent oscillation of the giant filament. This large-amplitude oscillation lasted for one cycle and its amplitude is $\sim$50 Mm in AIA 171 Å images and 72 Mm in Hα images, respectively. Such large-amplitude oscillations are often considered to be possible precursor signals of imminent filament eruptions (e.g., Y. Shen et al. 2014; J. Dai et al. 2023; Q. M. Zhang et al. 2024; Y. Zhang et al. 2024). After the horizontal magnetic field merged into the overlying giant filament structure and the appearance of prominent filament oscillation occurred, this giant filament abruptly entered its accelerating eruption phase from a quasi-static evolution phase. Based on the above observations and kinematic analysis, we conclude that a series of minifilament eruptions act as the last straw to break the quasi-static equilibrium of the giant filament, facilitating its final eruption.

3.5. Nonuniform Decay of Background Magnetic Fields

3D simulations of the flux cancellation model have demonstrated that the slow flux cancellation process is responsible for the buildup and ascent of the filament magnetic structure, and the onset of torus instability triggers the final eruption of an MFR at a critical height (G. Aulanier et al. 2010). Based on magnetic decay index analysis, we find that the decay of the background magnetic field in the region above the PIL exhibits obvious spatial nonuniformity. The 2D spatial distribution of decay index (Figures 4(B) and (C)) reveals that a torus-unstable domain appears at a very low height of 22 Mm above the photosphere near the middle segment of the PIL (where minifilaments erupted), and it extends to almost the whole PIL at the height of 65 Mm above the photosphere. The vertical spatial distribution of decay index along the PIL (Figure 4(E)) and line profiles of spatially averaged decay index (Figure 4(D)) also shows that the background magnetic field quickly decreases with height and this trend is most prominent above the middle part of the PIL. This nonuniformity of background magnetic fields naturally allows minifilaments to experience the torus instability due to the appearance of a low-lying torus-unstable domain above the middle segment of the long PIL, while preventing the giant filament from suffering the torus instability due to a high-lying torus-stable domain. A similar nonuniform decay of background magnetic fields has also been used to explain the onset of partial filament eruption in H. Chen et al. (2018).

Prior to eruptions, heights of the third minifilament and giant filament were measured as $\sim$12 Mm and 40 Mm, respectively (Figure 3(D); also see methods in Appendix B). The minifilaments are more likely supported by a short and straight

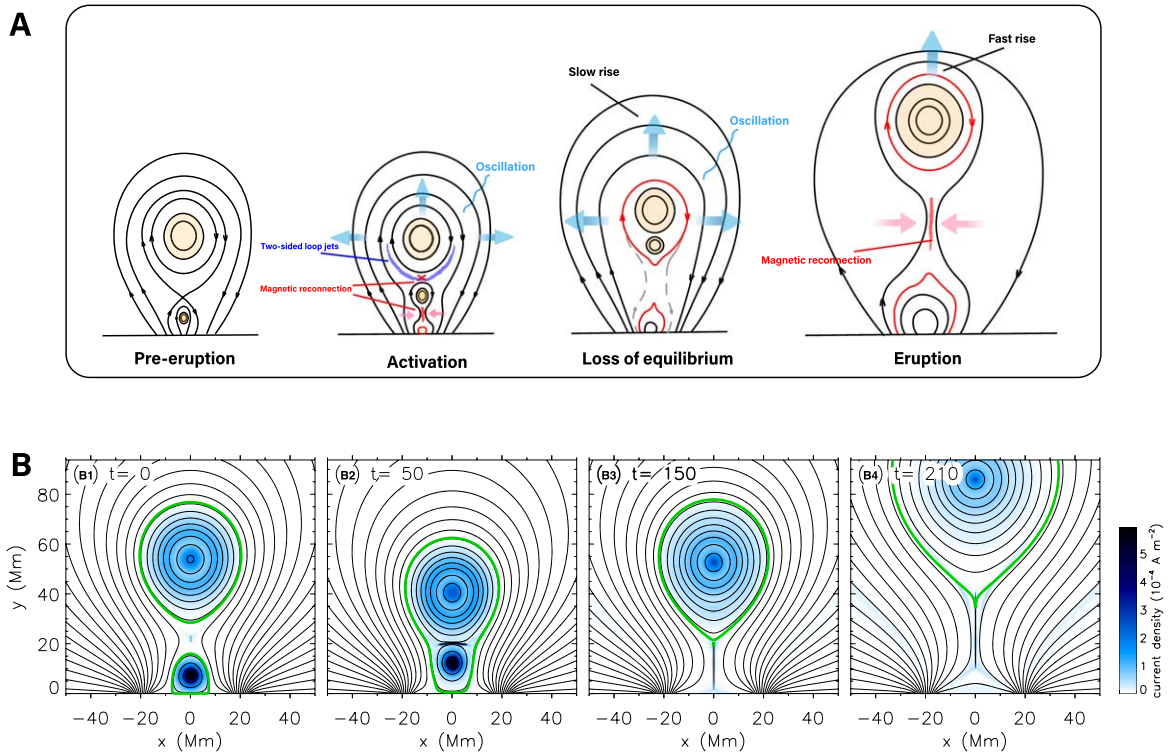

Figure 5. 2D schematic view and 2.5D MHD simulation of the coupling between miniature and giant filament eruptions. (A) In the pre-eruption phase, a mini-MFR and a giant MFR are both at the equilibrium state in the same filament channel, forming a double-decker system. In the activation phase, homologous mini MFRs subsequently lose equilibrium and erupt toward the overlying giant MFR, leading to the activation of the giant MFR. In this course, multiple magnetic interaction occurs between the magnetic field of the erupting mini-MFR and overlying giant MFR, including magnetic reconnection and flux feeding (or axial magnetic field merging), as well as oscillation. Reconnection occurs both ahead and behind the erupting mini-MFR, which leads to the two-sided loop jets and tiny standard flare arcades, respectively. In the loss-of-equilibrium phase, the flux merging process between mini- and giant MFRs facilitates the disruption of the whole system. In the eruption phase, a newly formed large flux rope becomes globally unstable and steps into its final eruption. (B) 2.5D MHD simulation reproducing the interaction, flux merging, oscillation, and the whole eruption of this double-decker MFR system. (B1) An initial double-decker flux rope system with a hyperbolic flux tube configuration. (B2) The flux merging between a small and a large flux rope and subsequent flux rope oscillation. (B3) The ascent of the newborn flux rope; (B4) The eruption of the newborn flux rope. The times indicated in panels (B1)–(B4) are in units of τ_A. The blue color depicts the distribution of the current density. The green curves indicate the boundary of the big and small flux ropes. An animation of Panel (B) is available in the online journal, depicting the 2.5D MHD simulation results. The animation shows the sequence from 0 to 130. The real-time duration of the animation is 13 s.

(An animation of this figure is available in the online article.)

flux rope configuration, which may even require a torus instability critical threshold of $\sim$1.0−1.1, or even lower than unity (B. Filippov 2021). In this case, they may become torus unstable at an even lower height, approximately 14 Mm above the photosphere (see Figure 4(D)). As a result of continuous flux convergence and cancellation at the middle segment of the long PIL, minifilaments are prone to losing their equilibrium at first. Subsequently, due to a trio of minifilament eruptions, the giant filament experiences sudden large-amplitude oscillations, propelling it to ascend to greater heights. Indeed, the 3D reconstruction result reveals that the giant filament attained a height of approximately 78 Mm at the onset time (around 19:54 UT). At this altitude, the decay index surpasses the critical threshold for torus instability, thereby allowing the sudden eruption of the giant filament.

3.6. Mechanism Behind the Physical Coupling between Miniature and Giant Filament Eruptions

Combining the above observations and analysis results, we conclude that a series of minifilament eruptions driven by an extremely weak flux cancellation break the initial equilibrium of an overlying giant filament via multiple interactions. We propose a scenario (depicted in Figure 5(A)) to explain the unique physical coupling between miniature and giant filament eruptions. Initially, the coexistence of minifilament and giant filament, which are of the same magnetic helicity, within the same filament channel, forms a double-decker MFR system (R. Liu et al. 2012). Due to the nonuniform decay of the background magnetic field, the high-lying giant filament remains in the torus-stable regime, while the background magnetic field above the minifilament decays rapidly, making it more prone to torus instability and eruption at a lower height. Under the continuous flux cancellation of small-scale magnetic fluxes at the middle segment of the PIL, minifilaments sequently form and erupt below the giant filament. The upward eruption of homologous minifilaments impacts the magnetic field at the bottom of the giant filament, triggering magnetic reconnection between the small and large flux ropes, as well as subsequent magnetic field merging between the flux ropes. Consequently, this reconnection process leads to the appearance of unique bidirectional coronal jets observed along the giant filament. Meanwhile, the erupting minifilament stretches the magnetic field upward, triggering subsequent standard flare reconnection and tiny two-ribbon flares. With multiple eruptions of minifilaments, similar processes repeat, and the merging of small and large MFRs results in sustained disturbance and large-amplitude oscillations of the giant filament above. Eventually, the newly formed large flux rope

becomes globally unstable and ascends into a higher torus-unstable regime, triggering a final global eruption and a two-ribbon flare at its source region. Recently, Y. Song et al. (2024) also reported a similar multi-filament eruption event in which a large-scale filament eruption was initiated by two preceding active region filaments pushing out from below. However, the authors stated that there was no strong evidence of magnetic reconnection between the different filaments. In contrast, our observations and magnetic field analysis provide a more comprehensive and clear insight into the formation and eruption of minifilaments and the subsequent magnetic interaction between the mini- and giant filaments.

By employing 2.5-dimensional (2.5D) MHD numerical simulations (methods in Appendix C), we have successfully reproduced the key physical processes observed in this scenario. The simulation results (see Figure 5(B) and associated movie) are consistent with our observational facts, illustrating that the small flux rope undergoes initial instability and ascends within a double-decker magnetic rope system. Subsequently, upon collision with the larger flux rope above, reconnection and magnetic field merging take place, resulting in the formation of a newly created large flux rope with an increased axial flux. (Note that in 2.5D simulations, magnetic field merging we observed often manifests as flux merging; therefore, the term "flux merging" refers to the same process in our discussion here and in Appendix C.) During this process, the newly formed large flux rope exhibits upward and downward oscillations. As the confinement of the background magnetic field remains unchanged, the augmented axial electric current within the large flux rope rapidly propels it upwards, abruptly leading to its disruption from a quasi-static equilibrium due to flux imbalance (Q. Zhang et al. 2020). This rising large flux rope then steps into its standard eruption, leaving a flare reconnection current sheet and associated post-flare loops behind.

4. Discussion

In the flux cancellation model (A. A. van Ballegooijen & P. C. H. Martens 1989), magnetic flux cancellations provide a necessary environment for the buildup of filament magnetic fields. In this model, flux cancellation is suggested as the submerging of field lines after magnetic reconnection between the adjacent opposite-polarity feet of different magnetic arcades above the PIL. This reconnection-cancellation process would gradually create a newborn MFR with increasing helical field lines and also reduce the overlying confinement. As such a process proceeds, the newborn MFR would meet a series of quasi-static equilibria at progressively higher altitudes. Eventually, it would reach a critical point of force balance, where the whole filament magnetic structure experiences a catastrophic loss of equilibrium and inevitably erupts. Until now, almost all of leading theories (e.g., S. K. Antiochos et al. 1999; J. Lin & T. G. Forbes 2000; T. Amari et al. 2003a; G. Aulanier et al. 2010; C. Jiang et al. 2021) and observational works (e.g., J. Zhang et al. 2001; J. Wang et al. 2017; R. Zheng et al. 2020; X. Yan et al. 2021) have exclusively considered the formation and eruption of isolated filaments. In particular, numerical simulations that related to flux cancellation have simply assumed that they are primarily governed by an idealized, uniform flux cancellation process (e.g., A. A. van Ballegooijen et al. 2000; T. Amari et al. 2003b; G. Aulanier et al. 2010; C. Xia et al. 2014). However, the real flux cancellation is more complex than an idealized process and their potential impacts on filament activity have been largely overlooked in the past. These subjective assumptions also hinder us from uncovering the potential physical connections between filament eruptions across different spatial-temporal scales.

Our finding of a physical coupling between miniature and giant filament eruptions within the same filament channel provides us a unique perspective to reconsider the traditional flux cancellation model of solar eruptions. The HMI observations reveal that from September 8 to 16, prolonged flux cancellation along the PIL exhibited significant temporal and spatial complexity that far exceeds the assumptions of an ideal uniform flux cancellation process commonly considered in most existing simulations and theories of solar eruptions. The key aspect of this complex flux cancellation is the gradual reduction in the size of the flux cancellation region over time, from a scale exceeding 100 Mm to a few Mm. Incorporating this fact allows for a more self-consistent understanding of all the reported phenomena above. First, this provides insight into why the giant filament and a series of minifilaments appear along the same PIL. Initially, flux cancellation at the scale of active regions establishes the large-scale filament channel and gives rise to the formation of the giant filament. Subsequently, the spatial region of flux cancellation gradually contracts to a few Mm, leading to the sequential formation of multiple minifilaments. Similar small-scale flux cancellation has been previously reported to be important for the formation and eruption of minifilaments at the base of coronal jets (N. K. Panesar et al. 2017, 2018; H. Chen et al. 2020). Second, this offers an explanation for the spatial nonuniformity in the decay of the background magnetic field above the PIL. Flux cancellation is closely associated with horizontal converging flows on the photosphere. Persistent converging flows are thought to be important in causing the gradual approaching of the photospheric footpoints of the background magnetic field, resulting in the elevation of the loop top of the background magnetic field above the PIL (T. G. Forbes & P. A. Isenberg 1991; P. A. Isenberg et al. 1993). In the later stages of the observations, the continuous flux convergence and cancellation primarily occur in the central region of the PIL. As a result, the decay of the background magnetic field along the PIL is most pronounced in the central portion, which provides a potential condition for the preferential eruption of minifilaments. Finally, this unveils a novel pathway through which the gradual evolution of the photospheric magnetic field initiates the abrupt eruption of large-scale filaments in the solar corona. The eruptions of minifilaments, driven by extremely weak flux cancellation within a spatial region of a few Mm, unexpectedly provide a novel avenue for small-scale magnetic activities at the solar surface to trigger the destabilization and eruption of the overlying giant filament.

In fact, there are some clues that the occurrence of miniature and giant filaments within a single filament channel may not be rare events (J.-Y. Yang et al. 2016; Y. Shen et al. 2019; A. C. Sterling et al. 2019; B. Yang et al. 2019; H. Wei et al. 2020; W. Teng et al. 2024; J. Yang et al. 2024), but the magnetic coupling of minifilaments to overlying giant filaments has been largely overlooked and solid evidence for their potential role in the triggering of solar eruptions has never been reported. A previous publication (Q. Zhang et al. 2014) has reported a prominence eruption driven by flux feeding from chromospheric fibrils, in which the flux feeding is quite similar to the horizontal flux merging reported here. The authors tended to attribute the origin of chromospheric fibrils to flux emergence below the overlying prominence, but the extra flux

emergence is not inherent to the formation of overlying solar prominences. In the current work, we first propose that both minifilaments and the overlying filament are homologous solar magnetic activities driven by the same physical process but only occur at different tempo-spatial scales. Within this unified framework, the formation and eruption of minifilaments and the larger overlying filament can be interpreted as self-similar MHD phenomena driven by a prolonged flux cancellation process. Meanwhile, the continuous transfer of mass, horizontal magnetic flux, as well as momentum from minifilament eruptions, which are driven by the gradual evolution of the photospheric magnetic field, represents a novel pathway to disrupt the force-free equilibrium of the overlying filament structure. Thus, our finding introduces a new and important ingredient to solar eruption models that was not encompassed within the traditional flux cancellation framework.

Acknowledgments

The authors sincerely thank the referee for the constructive suggestions. This work is supported by NSFC grants 12425301, 12103005, 12333009, 12073022, 12373115, 42188101, and 42174213 and the National Key R&D Program of China (nos. 2021YFA0718600). H.C.C. and X.C. are also supported by the Yunnan Key Laboratory of Solar Physics and Space Science (YNSPCC202210, 202205AG070009) and the Yunnan Provincial Basic Research Project (202401CF070165). Q.H.Z. is also supported by the Strategic Priority Research Program of the Chinese Academy of Sciences (XDB0560302). C.X. and Z.Y.H. are also supported by the Strategic Priority Research Program of the Chinese Academy of Sciences (XDB0560000). This work uses data from the CHASE mission supported by the China National Space Administration. SUTRI is a collaborative project conducted by the National Astronomical Observatories of CAS, Peking University, Tongji University, Xi'an Institute of Optics and Precision Mechanics of CAS, and the Innovation Academy for Microsatellites of CAS. AIA data and HMI Magnetic field data are courtesy of NASA/SDO, a mission of NASA's Living With a Star Program. STEREO EUVI data are courtesy of the STEREO/SECCHI consortium.

Appendix A
Filament Chirality and Magnetic Field Configuration

The giant filament was bred in a highly decayed active region, in which its photospheric vector magnetograms are too weak and discretized to perform a reliable coronal magnetic field extrapolation. Therefore, we judged the possible magnetic field configuration of the giant filament following an indirect method proposed based on the chirality and magnetic theoretical model of filaments (Y. Guo et al. 2010; P. F. Chen et al. 2014). This indirect method suggests that "if a sinistral filament has left-bearing (or right-bearing) barbs and right-skewed (or left-skewed) overlying arcades, it should be supported in an inverse-polarity MFR configuration (or a normal-polarity sheared arcade configuration); if a dextral filament, the correspondence is the opposite." This method has been widely used to determine the possible magnetic topologies of various types of filaments/prominences (e.g., Y. Ouyang et al. 2017; H. Chen et al. 2018). According to this indirect method, we can conclude that the giant filament exhibits sinistral characteristics and is supported by an inverse-polarity MFR. This conclusion is supported by several observational facts. First, when viewed from the positive-polarity side, the axial component field of the filament turns to the left, indicating its sinistral nature. Second, the giant filament displays left-bearing barbs, as depicted by the circles in Figure A1(A). Furthermore, during the eruption of the filament, two conjugate footpoints of its drainage were identified in the CHASE Doppler map, as shown by the arrows in Figure 2(B). It is evident that the two draining sites of the giant filament exhibit a right skewness of strapping arcades.

The minifilaments located below the giant filament, particularly the third one (Figure 1(H)), exhibit a distinct "S" shape, which suggests that they also possess a sinistral chirality (S. F. Martin 1998b). We examined the HMI vector magnetograms in the source region of minifilaments as it passed the center of the solar disk and found a notably higher average horizontal magnetic field compared to other sections of the giant filament's PIL. This thus allows a further analysis of magnetic topology and a possible magnetic field extrapolation in the source region of minifilaments. Fortunately, our observations indeed revealed the presence of bald patches above the forming site of the minifilament. This is clearly indicated by the red ellipse in Figure A1(J), where an orientation reversal of the horizontal magnetic field occurs at the photosphere (V. S. Titov et al. 1993). This reversal indicates that helical field lines are tangent from above to the photosphere in that region. Moreover, using this vector magnetogram as a boundary condition, the coronal magnetic field in the source region of minifilaments is extrapolated with the help of an NLFFF extrapolation code provided in the SSWIDL package. This code is developed based on an optimization method (M. S. Wheatland et al. 2000; T. Wiegelmann 2004; T. Wiegelmann et al. 2012). Our results of the NLFFF extrapolation, as depicted in Figures A1(K) and (L), further demonstrate the existence of a small-scale MFR with sinistral chirality above the forming site of the minifilaments. These results suggest that these minifilaments are associated with MFR configurations, which is in line with previous arguments on minifilament observations from H. Chen et al. (2020).

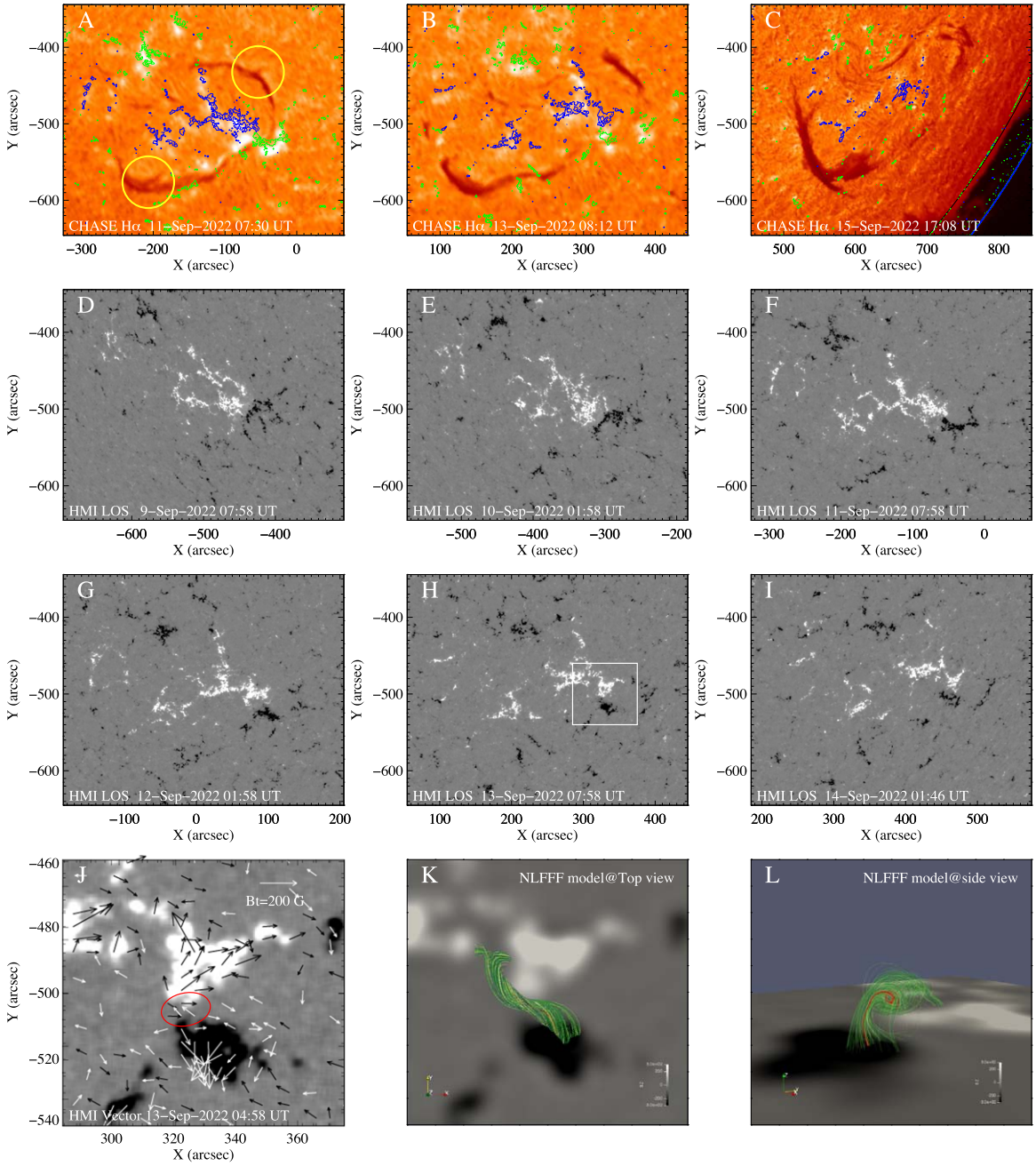

Figure A1. The long-term evolution of the filament channel, where mini- and giant filaments later erupt. (A)–(C) Selected Hα images taken by the CHASE, in which contours of simultaneous HMI magnetograms are overplotted at the level of ±300 Gauss. (D)–(I) HMI LOS magnetograms from 2022 September 9 to 2022 September 14. (J) HMI vector magnetogram in the region where minifilaments later form and erupt (see white rectangle in (H)). The black and white arrows represent the strength of positive and negative horizontal magnetic fields, respectively. The red ellipse highlights one plausible bold patch in this region. (K) Top view and (L) side view of the NLFFF model over this region. The background is HMI magnetograms with the level of ±300 Gauss. In panel (L), one red line highlights the helical trend of field lines.

Appendix B
3D Reconstruction and the Fitting of Height–Time Profiles

The dual-perspective EUV imaging observations provided by the STEREO-A/EUVI and SDO/AIA enable us to reconstruct the 3D topology and height of pre-eruption filaments and the two-sided loop jets, as shown in Figure B1. We chose the EUVI 304 images for 3D reconstruction. On 2022 September 15, the separation angle between STEREO-A and SDO was about 20°. The 3D reconstruction was conducted using the procedure *scc_measure.pro* in the SSWIDL package, which is developed by W. T. Thompson et al. (2012) and have been widely used in observational studies of solar filament eruptions (e.g., Y. Shen et al. 2019; H. Chen et al. 2021; Y. Duan et al. 2024). The procedure workflow is as follows: for each simultaneous time frame, two 304 Å images selected from STEREO-A/EUVI and SDO/AIA are displayed side by side, with a slight offset to account for the difference in light travel time from the Sun. The widget allows the user to zoom in on the region of interest in the two images, and optimize the appearance of the feature being measured by adjusting the color

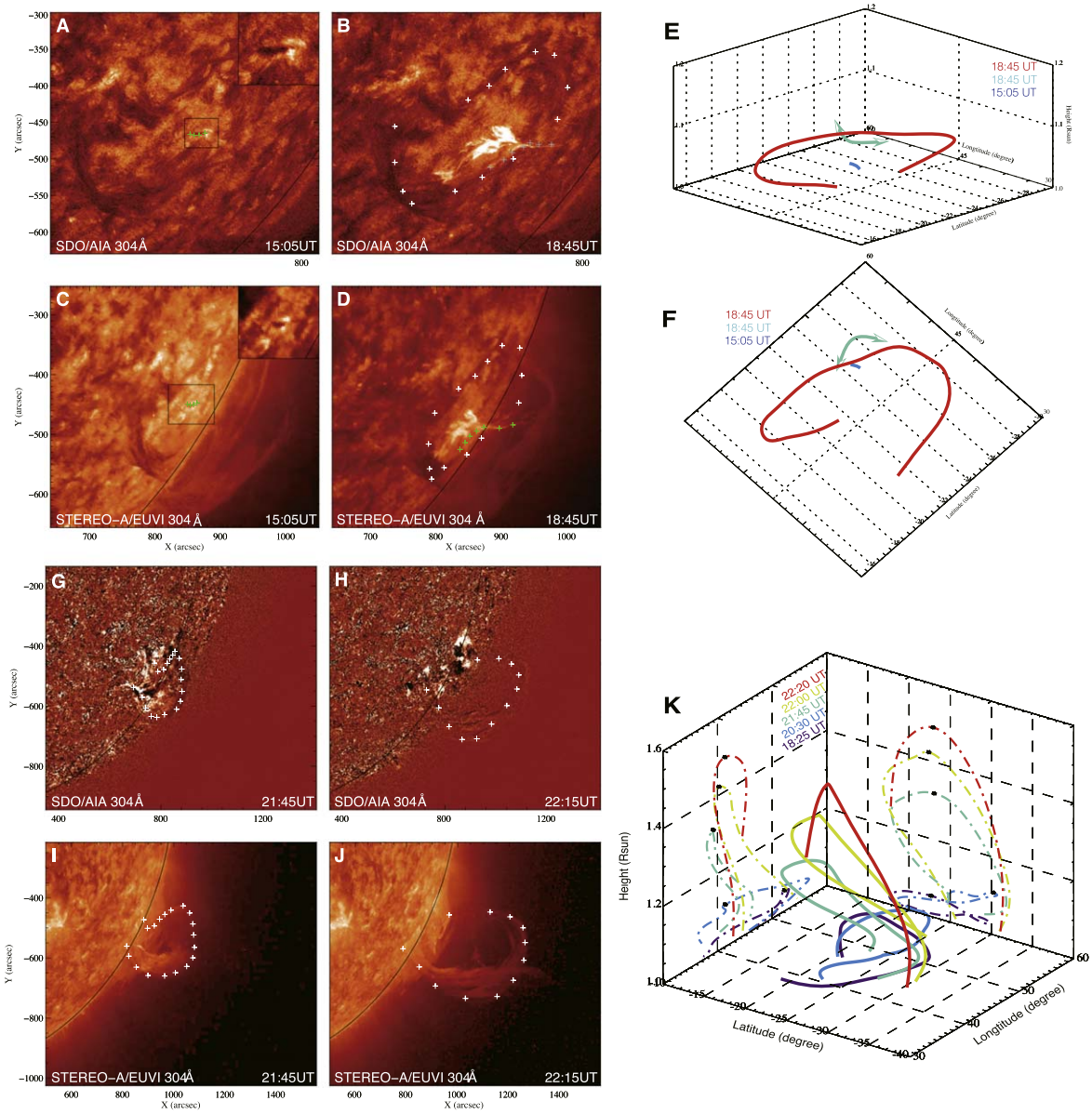

Figure B1. 3D reconstruction from dual-perspective SDO/AIA and STEREO-A/EUVI observations. (A)–(D) Dual-perspective snapshots of the third minifilament and the pre-eruption giant filament, as well as the two-side loop jets. A close-up view of the minifilament is shown at the right-up corner of (A) and (C), respectively. (E)–(F) 3D reconstructed morphology of the pre-eruption giant (red curve) and miniature filaments (blue curve), as well as two-side loop jets (cyan curve), viewed from two different perspectives. (G)–(J) Dual-perspective snapshots of the erupting giant filament at two different times. (K) 3D reconstruction results of the erupting giant filament at different times, and their projections on two different 2D planes. The black asterisks indicate the top of the filament's main axis, respectively.

table or data range. The user then can select a common feature appearing in both images with the cursor. Once a point is selected in the first image, the procedure calculates the 3D epipolar LOS of this selected point and then overplot the projection of this line onto the second image as a reference line. Along the reference line, the user can easily pinpoint the same feature in the second image with the cursor, which leads to another LOS calculation. As a result, the intersection of these two 3D epipolar lines determines the 3D location of the feature. For example, for the giant filament, the height of the top of the filament axis was measured over time (Figures B1(G) to (K)). Similarly, regarding the minifilament observed at 15:05 UT, its filament axis was reconstructed to estimate the approximate height of the homologous minifilament erupted at 18:05 UT; regarding the two-sided loop jet, its height and space trajectory were reconstructed in Figures B1(E) and (F).

Figure B2 presents the eruption of the giant filament and its height–time evolution observed from the perspective of STEREO-A. The height–time profiles that we obtained from the 3D reconstruction technique or time–distance diagram were well fitted by a function consisting of linear and exponential components (X. Cheng et al. 2013). This function can be defined as follows: $h(t) = ae^{\,b(t-t_0)} + c(t - t_0) + d$, where $h(t)$ is height, t is time, and a, b, c, d, and t_0 are five free parameters. Using the fitting technique, the onset time ($t_c = \frac{1}{b}\ln\left(\frac{c}{ab}\right) + t_0$) of the exponential acceleration of the giant filament eruption can be derived and its uncertainty can be estimated through Monte Carlo simulations. For each fitting, a critical height ($H_c = h(t_c)$) , where the impulsive acceleration begins, can also be determined from this fitting technique. In our study, this fitting technique was applied in Figures 3(E) and B2.

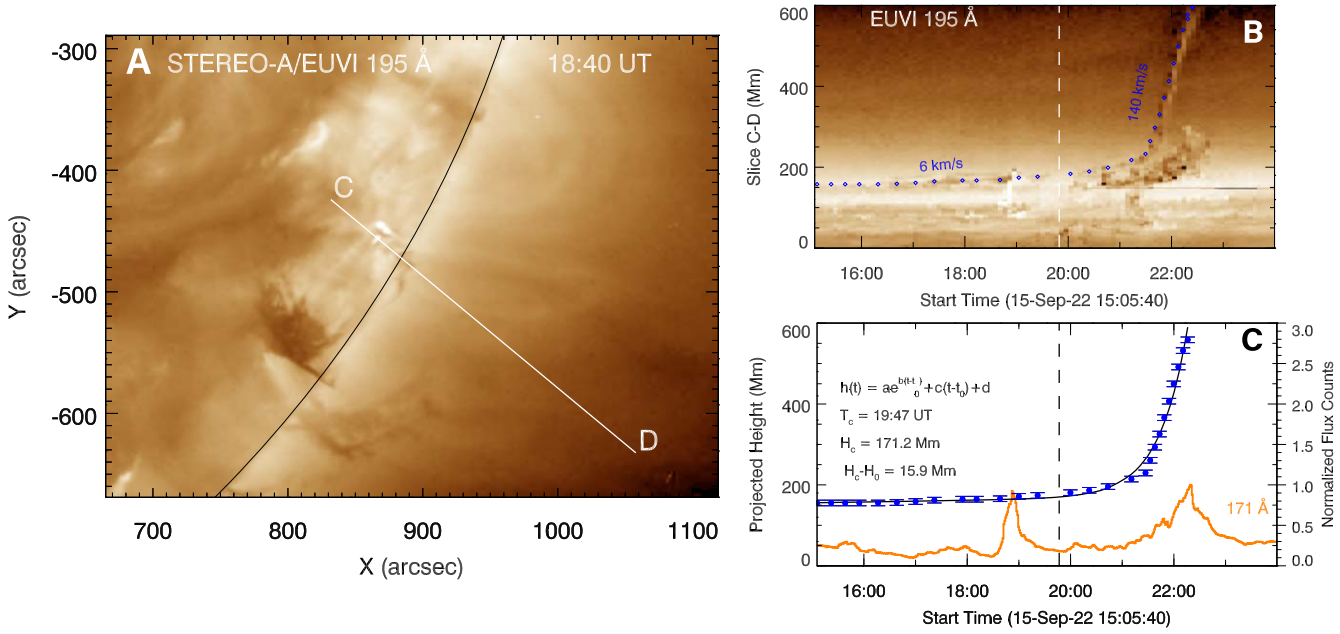

Figure B2. The eruption of the giant filament and its height–time evolution observed from the perspective of STEREO-A on 2022 September 15. (A) The STEREO-A/EUVI 195 Å image at 18:40 UT. The Slice CD represents the radial eruption path of the giant filament. (B) The spacetime diagram along slice CD, showing the height–time evolution of the giant filament eruption. (C) The height–time profile of the erupting giant filament and its fitting result. The AIA 171 Å flux variation computed in the source region (see the same FOV of Figure 3(E)) is also plotted. An animation of this figure is available in the online journal. The animation begins before the time sequence shown in panel (A), with the EUVI 195 Å images (panel (A)) spanning from 2022 September 15 15:00 UT to 23:55 UT. The duration of the animation is 4 s.

(An animation of this figure is available in the online article.)

Appendix C
Magnetic Field Decay Index Analysis

The occurrence of ideal MHD torus instability may lead to the rapid acceleration of the filament-hosting MFR. The torus instability only takes place when the filament-hosting MFR ascends into a torus-unstable domain, where the decay of background strapping magnetic fields exceeds a threshold so that strapping fields are insufficient to balance the upward hoop force. The decay of background magnetic fields can be characterized by a magnetic decay index. The magnetic decay index is calculated by the equation $n = -\partial \ln(B_h)/\partial \ln(h)$ (B. Kliem & T. Török 2006), where B_h represents the horizontal component of the background potential magnetic field, and h represents the height above the photosphere. For a semi-circular flux tube, its critical theoretical threshold is about 1.3–1.5, while for a straight flux tube, its critical theoretical threshold is about 1.0−1.1 (see B. Filippov 2021 and references therein). In the current work, we performed a potential field extrapolation for the whole source region of the giant and miniature filaments. While potential field extrapolation may not accurately capture the intricate magnetic structures of the filaments themselves, it has been proven to provide a reliable approximation to the overlying background magnetic field. Following the analysis method in H. Chen et al. (2018), in the current work, both the spatial distribution and spatial-averaged profile of the magnetic decay index were used to investigate the nonuniform decay of the background magnetic field above the PIL. The analysis results of the magnetic field decay index, calculated from magnetic field extrapolations on September 12 and 14, respectively. The results are generally consistent, but the magnetic field measurements on September 14 are subject to a more significant projection effect. Due to article length restrictions, only the results from September 12 are presented in Figure 4.

Appendix D
2.5D MHD Simulation

Our 2.5D MHD simulations are conducted following the basic settings and similar parameters as in Q. Zhang et al. (2021). The magnetic field is described by the equation: $B = \nabla \psi \times \hat{z} + B_z \hat{z}$, where ψ denotes the magnetic flux function and B_z represents the component of the magnetic field in the z-direction. All the magnitudes satisfy $\frac{\partial}{\partial z} = 0$, so that the evolution of magnetic field lines can be visualized in the x–y plane as isolines of ψ. The numerical domain is $0 < x < 200$ Mm, $0 < y < 300$ Mm, in which a symmetric condition is used in its left boundary ($x = 0$); increment equivalent extrapolation is used at the other boundaries (Q. Zhang et al. 2023). The background field is an open bipolar field with $B_z = 0$, whose magnetic charge are located at the lower photosphere within $-25 < x < -15$ Mm and $15 < x < 25$ Mm, respectively. An anomalous resistivity is used in the simulation to restrict magnetic reconnection within the regions of current sheets:

$$\eta = \begin{cases} 0, & \text{if } j < j_c, \\ (\eta_m \mu_0 v_0 L_0)\left(\frac{j}{j_c} - 1\right)^2, & \text{if } j > j_c. \end{cases} \quad \text{(D1)}$$

Here, $L_0 = 10^{-7}$ m, $\eta_m = 0.10$, $v_0 = 128.57$ km s^{-1}, $j_c = 4.45 \times 10^{-4}$ A m^{-2} is the critical current density, and μ_0 is the vacuum magnetic permeability. Starting from the initial state described in Q. Zhang et al. (2021), we initiated the emergence of a small flux rope from the lower boundary of the domain using

procedures similar to those outlined in Q. Zhang et al. (2021); the magnetic field strength within the emerging small rope is carefully tuned to be sufficiently weak, so that the small rope does not rise and merge with the preexisting coronal flux rope but sticks to the photosphere after the emergence. The magnetic fluxes of the two flux ropes are then adjusted by similar procedures as those in Y. Q. Hu et al. (2003), so as to achieve an equilibrium state, as illustrated in Figure 5(B1), where a minor/major flux rope is situated below/above the X-type magnetic structure, creating a double-decker flux rope configuration. This equilibrium state serves as the initial condition for our simulation. The azimuthal and axial flux of the major flux rope are set at $\Phi^m_{p0} = 11.2 \times 10^9\,\mathrm{Mx\,cm^{-1}}$ and $\Phi^m_{z0} = 48.5\times 10^{18}$ Mx, respectively, while the azimuthal and axial flux of the small rope are $\Phi^s_{p0} = 5.6 \times 10^9\,\mathrm{Mx\,cm^{-1}}$ and $\Phi^s_{z0} = 6.3\times 10^{18}$ Mx, respectively. With these initial conditions and the background configuration, numerical simulations are conducted to investigate the evolution of this double-decker flux rope system.

In our simulation, the magnetic fluxes of the major flux rope remain constant at Φ^m_{p0} and Φ^m_{z0}, while the azimuthal flux of the small flux rope is also held fixed at Φ^s_{p0}. In order to induce the subsequent eruption of the small flux rope, we implement a linear increase in its axial flux from Φ^s_{z0} to 6.7×10^{18} Mx over the period of 0–$5\tau_A$, where $\tau_A = 17.4$ s represents the characteristic Alfvén transit time. After $5\tau_A$, all the magnetic fluxes of the small and major ropes remain constant, allowing the system to evolve in a relaxed manner. As illustrated in Figure 5, the small flux rope gradually ascends and interacts with the major flux rope. With the ascent of the small flux rope, the major flux rope quickly undergoes a downward motion. By $t = 50\tau_A$, a horizontal current sheet emerges between the boundaries of the small and major flux ropes, where the current density distribution is depicted in blue (Figure 5(B2)). Subsequentially, the two flux ropes undergo reconnection and merge to form a larger newborn flux rope (Figure 5(B3)). This newly formed large flux rope ascends, creating a vertical current sheet in its path, and eventually erupts, as demonstrated in Figures 5(B3) and (B4).

ORCID iDs

Hechao Chen https://orcid.org/0000-0001-7866-4358
Hui Tian https://orcid.org/0000-0002-1369-1758
Quanhao Zhang https://orcid.org/0000-0003-0565-3206
Chuan Li https://orcid.org/0000-0001-7693-4908
Chun Xia https://orcid.org/0000-0002-7153-4304
Xianyong Bai https://orcid.org/0000-0003-2686-9153
Zhenyong Hou https://orcid.org/0000-0003-4804-5673
Kaifan Ji https://orcid.org/0000-0001-8950-3875

References

Airapetian, V. S., Barnes, R., Cohen, O., et al. 2020, IJAsB, 19, 136
Amari, T., Luciani, J. F., Aly, J. J., Mikic, Z., & Linker, J. 2003a, ApJ, 585, 1073
Amari, T., Luciani, J. F., Aly, J. J., Mikic, Z., & Linker, J. 2003b, ApJ, 595, 1231
Antiochos, S. K., DeVore, C. R., & Klimchuk, J. A. 1999, ApJ, 510, 485
Aulanier, G. 2014, in IAU Symp. 300, Nature of Prominences and their Role in Space Weather, ed. B. Schmieder, J.-M. Malherbe, & S. T. Wu (Cambridge: Cambridge Univ. Press), 184
Aulanier, G. 2021, NatAs, 5, 1096
Aulanier, G., Török, T., Démoulin, P., & DeLuca, E. E. 2010, ApJ, 708, 314
Bai, X., Tian, H., Deng, Y., et al. 2023, RAA, 23, 065014
Chen, H., Duan, Y., Yang, J., Yang, B., & Dai, J. 2018, ApJ, 869, 78
Chen, H., Hong, J., Yang, B., Xu, Z., & Yang, J. 2020, ApJ, 902, 8
Chen, H., Yang, J., Hong, J., Li, H., & Duan, Y. 2021, ApJ, 911, 33
Chen, P. F. 2011, LRSP, 8, 1
Chen, P. F., Harra, L. K., & Fang, C. 2014, ApJ, 784, 50
Cheng, X., Zhang, J., Ding, M. D., et al. 2013, ApJL, 769, L25
Cheng, X., Zhang, J., Kliem, B., et al. 2020, ApJ, 894, 85
Collier Cameron, A. 1996, in IAU Symp. 176, Stellar Surface Structure, ed. K. G. Strassmeier & J. L. Linsky (Dordrecht: Kluwer), 449
Dai, J., Zhang, Q., Qiu, Y., et al. 2023, ApJ, 959, 71
Duan, Y., Shen, Y., Tang, Z., Zhou, C., & Tan, S. 2024, ApJ, 968, 110
Fan, Y. 2018, ApJ, 862, 54
Filippov, B. 2021, MNRAS, 503, 3926
Forbes, T. G., & Isenberg, P. A. 1991, ApJ, 373, 294
Guo, Y., Schmieder, B., Démoulin, P., et al. 2010, ApJ, 714, 343
Hong, J., Jiang, Y., Zheng, R., et al. 2011, ApJL, 738, L20
Hou, Y., Li, C., Li, T., et al. 2023, ApJ, 959, 69
Hou, Z., Tian, H., Madjarska, M. S., et al. 2024, A&A, 687, A190
Howard, R. A., Moses, J. D., Vourlidas, A., et al. 2008, SSRv, 136, 67
Hu, Y. Q., Li, G. Q., & Xing, X. Y. 2003, JGRA, 108, 1072
Isenberg, P. A., Forbes, T. G., & Demoulin, P. 1993, ApJ, 417, 368
Jiang, C., Feng, X., Liu, R., et al. 2021, NatAs, 5, 1126
Jiang, Y., Bi, Y., Yang, J., et al. 2013, ApJ, 775, 132
Jing, J., Yurchyshyn, V. B., Yang, G., Xu, Y., & Wang, H. 2004, ApJ, 614, 1054
Kliem, B., & Török, T. 2006, PhRvL, 96, 255002
Kotani, Y., Shibata, K., Ishii, T. T., et al. 2023, ApJ, 943, 143
Lemen, J. R., Title, A. M., Akin, D. J., et al. 2012, SoPh, 275, 17
Li, C., Fang, C., Li, Z., et al. 2022, SCPMA, 65, 289602
Li, D., Bai, X., Tian, H., et al. 2023, A&A, 675, A169
Li, L., Tian, H., Chen, H., et al. 2023, ApJ, 949, 66
Lin, J., & Forbes, T. G. 2000, JGR, 105, 2375
Liu, R., Kliem, B., Török, T., et al. 2012, ApJ, 756, 59
Mackay, D. H., Karpen, J. T., Ballester, J. L., Schmieder, B., & Aulanier, G. 2010, SSRv, 151, 333
Martin, S. F. 1998a, SoPh, 182, 107
Martin, S. F. 1998b, in ASP Conf. Ser. 150, IAU Coll. 167: New Perspectives on Solar Prominences, ed. D. F. Webb, B. Schmieder, & D. M. Rust (San Francisco, CA: ASP), 419
Moore, R. L., Sterling, A. C., Hudson, H. S., & Lemen, J. R. 2001, ApJ, 552, 833
Ouyang, Y., Zhou, Y. H., Chen, P. F., & Fang, C. 2017, ApJ, 835, 94
Panesar, N. K., Sterling, A. C., & Moore, R. L. 2017, ApJ, 844, 131
Panesar, N. K., Sterling, A. C., & Moore, R. L. 2018, ApJ, 853, 189
Parenti, S. 2014, LRSP, 11, 1
Pesnell, W. D., Thompson, B. J., & Chamberlin, P. C. 2012, SoPh, 275, 3
Qiu, Y., Rao, S., Li, C., et al. 2022, SCPMA, 65, 289603
Raouafi, N. E., Georgoulis, M. K., Rust, D. M., & Bernasconi, P. N. 2010, ApJ, 718, 981
Scherrer, P. H., Schou, J., Bush, R. I., et al. 2012, SoPh, 275, 207
Schmieder, B., Démoulin, P., & Aulanier, G. 2013, AdSpR, 51, 1967
Schrijver, C. J. 2010, ApJ, 710, 1480
Shen, Y., Liu, Y. D., Chen, P. F., & Ichimoto, K. 2014, ApJ, 795, 130
Shen, Y., Qu, Z., Yuan, D., et al. 2019, ApJ, 883, 104
Shibata, K., & Magara, T. 2011, LRSP, 8, 6
Song, Y., Su, J., Zhang, Q., et al. 2024, SoPh, 299, 85
Sterling, A. C., Harra, L. K., Moore, R. L., & Falconer, D. A. 2019, ApJ, 871, 220
Sterling, A. C., Moore, R. L., Falconer, D. A., & Adams, M. 2015, Natur, 523, 437
Su, Y., & van Ballegooijen, A. 2012, ApJ, 757, 168
Sun, Z., Li, T., Tian, H., et al. 2023, ApJ, 953, 148
Tan, S., Shen, Y., Zhou, X., et al. 2023, MNRAS, 520, 3080
Teng, W., Su, Y., Liu, R., et al. 2024, ApJ, 970, 100
Thompson, W. T., Kliem, B., & Török, T. 2012, SoPh, 276, 241
Tian, H. 2017, RAA, 17, 110
Tian, H., Xu, Y., Chen, H., et al. 2023, ScSnT, 53, 2021
Titov, V. S., Priest, E. R., & Demoulin, P. 1993, A&A, 276, 564
Török, T., Kliem, B., & Titov, V. S. 2004, A&A, 413, L27
van Ballegooijen, A. A., & Martens, P. C. H. 1989, ApJ, 343, 971
van Ballegooijen, A. A., Priest, E. R., & Mackay, D. H. 2000, ApJ, 539, 983
Wang, J., Li, W., Denker, C., et al. 2000, ApJ, 530, 1071
Wang, J., Yan, X., Qu, Z., Xue, Z., & Yang, L. 2017, ApJ, 839, 128
Wei, H., Huang, Z., Hou, Z., et al. 2020, MNRAS, 498, L104

Wheatland, M. S., Sturrock, P. A., & Roumeliotis, G. 2000, ApJ, 540, 1150
Wiegelmann, T. 2004, SoPh, 219, 87
Wiegelmann, T., Thalmann, J. K., Inhester, B., et al. 2012, SoPh, 281, 37
Wyper, P. F., Antiochos, S. K., & DeVore, C. R. 2017, Natur, 544, 452
Xia, C., Keppens, R., & Guo, Y. 2014, ApJ, 780, 130
Yan, X., Wang, J., Guo, Q., et al. 2021, ApJ, 919, 34
Yang, B., Yang, J., Bi, Y., et al. 2019, ApJ, 887, 220
Yang, J., Chen, H., Hong, J., Yang, B., & Bi, Y. 2024, ApJ, 964, 7
Yang, J.-Y., Jiang, Y.-C., Yang, B., Hong, J.-C., & Xu, Z. 2016, RAA, 16, 3
Zhang, J., Wang, J., Deng, Y., & Wu, D. 2001, ApJL, 548, L99
Zhang, Q., Cheng, X., Liu, R., et al. 2023, FrASS, 9, 434
Zhang, Q., Liu, R., Wang, Y., et al. 2014, ApJ, 789, 133
Zhang, Q., Liu, R., Wang, Y., et al. 2021, A&A, 647, A171
Zhang, Q., Wang, Y., Liu, R., et al. 2020, ApJL, 898, L12
Zhang, Q. M., Lin, M. S., Yan, X. L., et al. 2024, MNRAS, 533, 3255
Zhang, Y., Zhang, Q., Song, D.-c., & Ji, H. 2024, ApJ, 963, 140
Zheng, R., Chen, Y., Huang, Z., et al. 2018, ApJ, 861, 108
Zheng, R., Chen, Y., Wang, B., Song, H., & Cao, W. 2020, A&A, 642, A199
Zhou, X., Shen, Y., Yan, Y., et al. 2024, ApJ, 968, 85
Zwaan, C. 1987, ARA&A, 25, 83